Available online at www.sciencedirect.com

ScienceDirect

International Journal of Solids and Structures 44 (2007) 5163–5181

INTERNATIONAL JOURNAL OF SOLIDS and STRUCTURES

www.elsevier.com/locate/ijsolstr

Damage accumulation and fracture initiation in uncracked ductile solids subject to triaxial loading

Liang Xue *

Department of Mechanical Engineering, Massachusetts Institute of Technology, 77 Massachusetts Avenue, 5-011, Cambridge, MA 02139, USA

Received 26 July 2005; received in revised form 16 November 2006
Available online 29 December 2006

Abstract

A damage plasticity model for ductile fracture is proposed. This model is established on the cylindrical coordinate system of principal stress space. Experimental results show that fracture initiation in uncracked ductile solids is sensitive to the hydrostatic pressure and dependent on the Lode angle. The joint effects of pressure and Lode angle define a *fracture envelope* in principal stress space. Plastic deformation induced damage is calculated by an integral of the damage rate measured at current loading and deformation status with respect to the fracture envelope. A power law damage rule is proposed to characterize the nonlinearity in damage accumulation. A damage-related weakening factor is adopted to describe the material deterioration. The material parameters are calibrated from standard laboratory tests. The proposed model is numerically implemented. Four simulations with emphasis on crack path prediction are presented.

Keywords: Ductile fracture; Hydrostatic pressure; Lode dependence; Damage plasticity model

1. Introduction

The ductile failure of structures usually consists of three phases: (a) accumulation of damage; (b) initiation of fracture; and (c) crack propagation. One way to think of fracture initiation is to consider it as the result of the accumulation of ductile plastic damage (Lemaître, 1985). Microscopically, such damages associated with void nucleation, growth and coalescence, shear band movement and the propagation of micro-cracks (McClintock, 1968; Rice and Tracey, 1969). Macroscopically, degradation of the material exhibits a decrease of the material stiffness, strength and a reduction of the remaining ductility (Lemaître, 1992). These physical changes are often used as indicators to predict the onset of fracture, either based on the current value or in a cumulative fashion. In continuum damage mechanics, the material deterioration is described by an internal variable of the so-called ‘‘damage.’’ In many applications, the damage can be considered isotropic but still give good predictions and, therefore, is assumed as a scalar quantity herein. Damage should be distinguished from

* Tel.: +1 617 253 6055; fax: +1 617 253 8125.
E-mail address: xue@alum.mit.edu

0020-7683/$ - see front matter © 2006 Elsevier Ltd. All rights reserved.
doi:10.1016/j.ijsolstr.2006.12.026

the ductility or the fracture strain in that damage is an internal quantity and often cannot be measured directly. To utilize cumulative damage as a criterion to predict the onset of fracture, the relationship between damage and some measurable quantities has to be established.

Various fracture models have been proposed to quantify the damage associated with material deformation and are used to predict fracture initiation, (e.g. Cockcroft and Latham, 1968; Gurson, 1977; Johnson and Cook, 1985; McClintock, 1968; Rice and Tracey, 1969; Wilkins et al., 1980).

Using conventional J_2 plasticity, cumulative strain damage models describe the damage and its accumulation in a phenomenological way. The material is considered to be homogenous and the plastic deformation is isochoric. Acknowledging the damage is associated with the plastic deformation, a cumulative strain damage fracture model accesses the damage using an integral of a weighting function with respect to plastic strain increments. For many materials, such as poly-crystalline metals, in the moderate range of pressure and temperature, the damage is a monotonically increasing function if no recrystallization occurs.

2. Formulation of a new damage plasticity model

Material fracture is characterized by a complete loss of its load carrying capacity and deformability. We propose a damage plasticity model which incorporates the pressure and Lode angle dependence of ductile fracture. The evolution of damage is considered to be a non-linear process. The material deterioration is included by a weakening factor on the material strength.

Experimental work shows that compressive pressure increases the ductility in many ductile and brittle materials, such as metals (Bridgman, 1952; Lewandowski and Lowhaphandu, 1998; Pugh et al., 1960; Spitzig, 1990) and rocks (von Karman, 1911; Mogi, 1972). Hydrostatic tension speeds up both the void nucleation-growth-coalescence process and the shear band slip movement; while compressive pressure slows down such actions. The Lode angle characterizes the deviatoric stress state on a hydrostatic plane. The Lode angle dependence of ductile fracture is less studied compared with the well-known pressure sensitivity. Experiments suggest that the fracture strain in the plane strain condition is less than that in the axisymmetric tension case (Clausing, 1970; McClintock et al., 1971; Mogi, 1967). Fracture is a sudden change in the configuration, but damage is a cumulative process.

2.1. Hypothesis

We start by distinguishing the matrix material, which remains undamaged throughout the plastic deformation all the way to the onset of fracture, and the damaged material, which is the matrix containing solid that also includes damages, such as micro voids, micro cracks, etc. The matrix stress–strain relationship is described by a strain hardening function, i.e.

$$\sigma_{\mathrm{M}} = \sigma_{\mathrm{M}}(\varepsilon_{\mathrm{p}}), \tag{1}$$

where σ_{M} is the equivalent matrix stress and ε_{p} is the plastic strain. Here, we assume the material to be isotropic and to follow von Mises yield condition.

The material deterioration can be characterized by a weakening factor, which is a function of the so-called damage,

$$\sigma_{\mathrm{eq}} = w(D)\sigma_{\mathrm{M}}, \tag{2}$$

where σ_{eq} is the equivalent stress of the applied stress and $w(D)$ is the weakening factor defined on the damage variable D.

In the present paper, we adopt the *relative loss of deformability* of the ductile solids as the damage variable. If a body fractures after repeating the same deformation 10 times, the damage is considered to be 0.1 each time. An immediate corollary of this definition of damage is that the material is intact when $D = 0$ and is fully damaged or fractured at $D = 1$.

The damage evolves when the solid materials subjected to plastic loading. We use the three dimensional space of the principal stresses to consider the damage process. The principal stresses are represented in the cylindrical coordinate system denoted by (p, θ, σ_{eq}), where p is the hydrostatic pressure, θ is the azimuthal angle on the octahedral plane and σ_{eq} is the von Mises equivalent stress.

The fundamental assumption made in deriving this model is the following:

"*The damaging process is self-similar with respect to the ratio of the plastic strain to the fracture strain on any deviatorically proportional loading path at any given pressure.*"

By making this hypothesis, we fix the pressure and the azimuthal angle on the octahedral plane. The damage evolution is now dependent only on the ratio of the plastic strain to the fracture strain. The above "*self-similarity*" hypothesis can be formally written as

$$D = f\left(\frac{\varepsilon_p}{\varepsilon_f}\right), \tag{3}$$

where D is the accumulated damage and ε_f is the fracture strain on the given path identified by p and θ. The rate form of Eq. (3) is

$$\dot{D} = \frac{\partial f\left(\frac{\varepsilon_p}{\varepsilon_f}\right)}{\partial\left(\frac{\varepsilon_p}{\varepsilon_f}\right)} \frac{\dot{\varepsilon}_p}{\varepsilon_f}. \tag{4}$$

We assume the ductile damage is due to plastic straining, therefore, the partial derivatives with respect to the pressure p and the azimuthal angle θ do not appear in Eq. (4) since $\partial p/\partial\varepsilon_p = 0$ and $\partial\theta/\partial\varepsilon_p = 0$. In Eq. (4), the normalization denominator ε_f is defined by the pressure and the azimuthal angle θ, i.e.

$$\varepsilon_f = \varepsilon_f(p, \theta). \tag{5}$$

Assuming the effects of the hydrostatic pressure and the azimuthal angle are independent of each other, the equivalent failure strain can be further decomposed as

$$\varepsilon_f = \varepsilon_{f0}\mu_p(p)\mu_\theta(\theta), \tag{6}$$

where ε_{f0} is a material constant (a reference fracture strain), $\mu_p(p)$ and $\mu_\theta(\theta)$ represents the effect of the hydrostatic pressure and the deviatoric state, respectively. When both μ_p and μ_θ take the value of unity, the present model degenerates to the constant failure strain criterion.

The fracture envelope shows the relative extent of ductility for a given pressure and azimuthal angle. However, in practical situations, all three stress invariants vary along the plastic loading path. The actual damage is the result of progressive accumulation from the loading history of varying pressure and azimuthal angle. Therefore, the damage has to be described by a history variable.

Based on these assumptions, the constitutive relationship of the material is described by a set of four equations, Eqs. (1), (2), (4) and (6). These equations form the theoretical basis of the proposed damage plasticity model. The internal variables are the plastic strain and the damage. The input functions for the material are these five curves: $\sigma_M(\varepsilon_p)$, $w(D)$, $f(\frac{\varepsilon_p}{\varepsilon_f})$, $\mu_p(p)$ and $\mu_\theta(\theta)$. The method to calculate the damage accumulation is called "*cylindrical decomposition*" hereafter.

2.2. Damage evolution

There is a wide spectrum of definitions of damage including micro void volume fraction and the reduction of stiffness etc. The critical amount of damage in the cumulative strain damage models is often thought of as a calibration constant depending on the weighting function of the integral. However, it can always be normalized such that the fracture criterion can be considered as the fracture occurring when the damage reaches unity.

The simplest form of a damage accumulation rule is a linear function, which in turn means the damage is proportional to the equivalent plastic strain, i.e.

$$\dot{D} = \frac{1}{\varepsilon_f}\dot{\varepsilon}_p \tag{7}$$

which is used by many researchers, e.g. Johnson and Cook (1985). Moreover, the damage is not necessarily linear with respect to the equivalent plastic strain on a constant pressure or a constant stress triaxiality path

(Bonora and Newaz, 1998). For instance, Børvik et al. (2001) considered that there exists a threshold of plastic strain below which no damage is accumulated.

The present definition of damage carries an analogue to reversed and repeated loading. It has been shown by experiments that low cycle fatigue is a plasticity-dominated phenomenon and it appears to be dependent mainly upon the ductility of metals (Libertiny, 1967; Suresh, 1998). By using the Palmgren–Miner rule and further assuming that the forward motion and the backward motion (i.e. $\varepsilon_{ij}^{\text{backward}} = -\varepsilon_{ij}^{\text{forward}}$) induce the same amount of damage, a power law damage accumulation rule is derived from the relationship of the so-called "$\Delta\varepsilon_p$–N" curve, where $\Delta\varepsilon_p$ is the range of the cyclic equivalent plastic strain, N is the number of cycles to fracture initiation.

The relationship between the applied plastic strain and the number of cycles to failure ($\Delta\varepsilon_p$–N curve) can be described by the so-called Manson–Coffin relationship (Coffin, 1954; Manson et al., 1954) for a number of materials, i.e.

$$\Delta\varepsilon_p \cdot N^{k_0} = C, \tag{8}$$

where C and k_0 are material constants.

The low cycle fatigue type of loading can be characterized by the ratio of the minimum to the maximum strain, i.e. $R = \varepsilon_{\min}/\varepsilon_{\max}$. Let us consider the special case of $R = 0$. The first monotonic loading path is considered as a half cycle, i.e. $N = \frac{1}{2}$. The Manson–Coffin relationship appears to be linear on a log–log scale of $\Delta\varepsilon_p$ and N.

For each half cycle, the damage associated with the strain increment $\Delta\varepsilon_p$ is approximately

$$D = \frac{1}{2N}. \tag{9}$$

Differentiating Eqs. (8) and (9) and letting $m = 1/k_0$, the damage evolution law can be derived as a power law function, i.e.

$$\mathrm{d}D = m\left(\frac{\varepsilon_p}{\varepsilon_f}\right)^{(m-1)}\frac{1}{\varepsilon_f}\mathrm{d}\varepsilon_p, \tag{10}$$

where ε_f is the fracture strain from monotonic loading. Integrating Eq. (10) from intact state, the damage evolution is a power function on a deviatorically proportional loading path of constant pressure, i.e.

$$D\left(\frac{\varepsilon_p}{\varepsilon_f}\right) = \left(\frac{\varepsilon_p}{\varepsilon_f}\right)^{\mathrm{m}}. \tag{11}$$

Typical values of the exponent k_0 in Eq. (8) vary from 0.33 to 0.75 for many metals, e.g. aluminum alloy, steel and brass etc. (Osgood, 1982), which means $m = 1.3$–3. For instance, the exponent m for 2024-T6 aluminum alloy can be determined by fitting the experimental $\Delta\varepsilon_p$–N curve from Coffin and Tavernelli (1959) and $m = 1.73$ as shown in Fig. 1.

It should be noted that a large amount of experimental work on the low cycle fatigue was done for push–pull (tension–compression) loading cycles, e.g. (Coffin, 1958, 1967; Manson et al., 1963). Under such conditions, the hydrostatic pressure experienced in a full cycle changes according to the strain state. However, in the torsion test, the hydrostatic stress is always zero. Halford et al. (1962) did low cycle torsion fatigue tests on several metals and found the same linear relationship on the log–log scale of the equivalent plastic strain versus the number of cycles to fracture.

2.3. Material weakening

The damage-induced material weakening is introduced into the constitutive model by coupling the yield function and associated flow rule with the damage. Following the continuum damage mechanics, the yield condition is

$$\Phi = \sigma_{eq}^2 - [(1 - D_s)\sigma_M]^2 \geqslant 0, \tag{12}$$

where σ_M is the yield strength for the matrix material and σ_{eq} is the applied stress on the damaged material. The damage D_s represents the decrease of the effective load carrying area in the material (Kachanov, 1958).

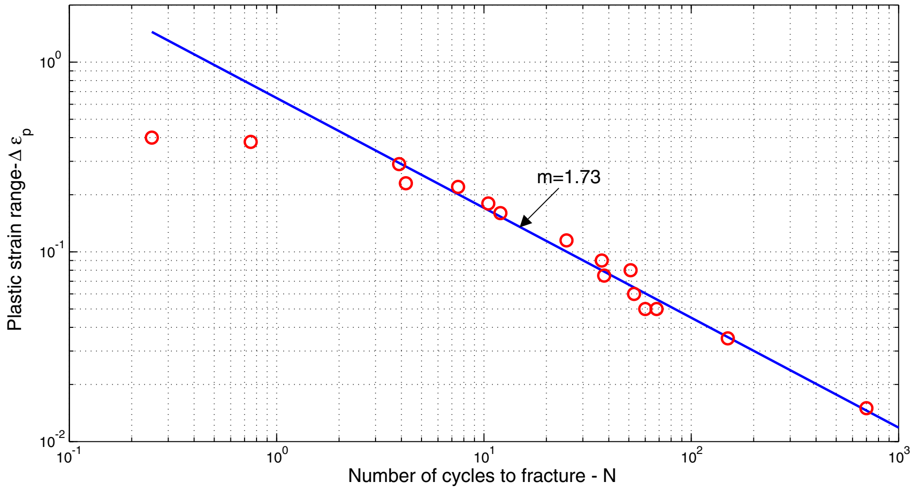

Fig. 1. A linear fit for the $\Delta\varepsilon_p$–N relationship for the aluminum alloy 2024-T6. Experimental data from Coffin and Tavernelli (1959).

Following the hypothesis of strain equivalence (Lemaître and Chaboche, 1978), the strain for a damaged material is assumed to be equal to the undamaged material and the stress of the damaged material is replaced by the effective stress. Material hardening is described by the hardening behavior of the matrix material, which is represented by the σ_M in Eq. (12); while material softening is represented by the multiplication factor of $(1 - D_s)$. We assume the elastic modulus decreases at the same rate, i.e.

$$E = (1 - D_s)E_0, \tag{13}$$

where E is the current elastic modulus and E_0 is the original Young's modulus. The two damage quantities D and D_s are referred to as the ductile damage and the stiffness damage. Lemaître and Dufailly (1987) measured the stiffness damage and showed increasing rate of stiffness loss when matrials approach fracture point. In general, the ductile damage and the stiffness damage are not necessarily the same. For instance, a power law relationship $D_s = D^{\beta_1}$ is adopted in Xue (2007), where β_1 is a material constant and $\beta_1 > 1$. In the present paper, the stiffness damage and the ductile damage are assumed to be the same by a first order approximation, i.e. $D_s = D$.

2.4. Hydrostatic pressure sensitivity

Materials become more ductile as they experience high compressive pressures (Bridgman, 1952). For porous materials, the equivalent fracture strain is found to decrease exponentially with respect to increasing stress triaxiality, i.e. the ratio of the mean stress to the equivalent stress (Johnson and Cook, 1985; Norris et al., 1978). Notched round bars experience higher triaxiality than un-notched round bars when subjected to tension. The fracture strains of notched specimens are found to be less than those of the un-notched round bars (Hancock and Mackenzie, 1976; Holland et al., 1990). The relationship between the plastic strain at fracture and the hydrostatic pressure is determined from a particular load condition – the generalized tension.

One of the most comprehensive studies was carried out by Bridgman (1952), who tested the effect of hydrostatic pressure on the material fracture strain for several types of armor steels. Bridgman used round bars and pulled them in a pressure chamber. The round bar specimens are in a uniaxial tension condition superimposed on which is a hydrostatic pressure. Because the two lateral principal stress components remain identical at the center line for the axisymmetric specimen, Lode angle remains −30° at the center of the neck throughout his experiments. The ratio of the cross-sectional area at the neck after fracture to the initial cross-sectional area was found to decrease with respect to the superimposed confining pressure.

In addition to the confining pressure, a tensile force is applied on the longitudinal direction. Bridgman defines the flow stress σ_{flow} as the difference between the stress in the longitudinal direction and the confining pressure (Bridgman, 1952), i.e.

$$\sigma_{\text{flow}} = \sigma_{\text{long}} - p_{\text{conf}}, \tag{14}$$

where σ_{long} is the true stress in the pulling direction and σ_{conf} is the confining pressure.

By observing the test results, the relationship of the fracture strain to the confining pressure may be expressed as a power law, viz.

$$\frac{A_{\text{f}}}{A_0} = \frac{A_{\text{f0}}}{A_0} \cdot \left(1 - \frac{p_{\text{conf}}}{p_{\text{lim}}}\right)^{\bar{q}}, \tag{15}$$

where $\bar{q}$ is a material constant that fits the experimental data best, A_0 is the original cross-sectional area, A_{f} is the cross-sectional area after fracture at the neck, A_{f0} is the cross-sectional area after fracture at the neck at atmospheric pressure and p_{lim} is a limiting pressure beyond which the material will not fail in the uniaxial tensile condition.

Taking logarithms of both sides of Eq. (15), one gets[1]

$$\varepsilon_{\text{f}} = \varepsilon_{\text{f0}} \left[1 - q \log\left(1 - \frac{p}{p_{\text{lim}}}\right)\right], \tag{16}$$

where ε_{f} is the fracture strain at the confining pressure p, $\varepsilon_{\text{f0}} = \log \frac{A_0}{A_{\text{f0}}}$ is the uniaxial tensile failure strain without confining pressure, and $q = \frac{\bar{q}}{\varepsilon_{\text{f0}}}$. Therefore, the pressure dependence function $\mu_{\text{p}}(p)$ becomes

$$\mu_{\text{p}}(p) = 1 - q \log\left(1 - \frac{p}{p_{\text{lim}}}\right). \tag{17}$$

There are two concerns about Eq. (17). First, for numerical implementation, it is not feasible to use the confining pressure for triaxial loading cases. Therefore, the confining pressure is replaced by the hydrostatic pressure and the form of Eq. (17) is retained, except that the material constants are re-calibrated for the hydrostatic pressure.

The second concern is the hydrostatic pressure is not constant in the course of the Bridgman tests. Thus, an approximate method of averaging the experienced hydrostatic pressure over the plastic loading path is used to calibrate the material parameters.

The average hydrostatic pressure experienced in the course of pulling is illustrated in Fig. 2. The equivalent stress path on the σ_{eq}–p plane is shown as the thick solid line. The mean hydrostatic pressure, p_{ave}, along the entire loading path is estimated to be

$$p_{\text{ave}} = p_{\text{conf}} - \frac{\sigma_{\text{flow}}}{6}. \tag{18}$$

The estimated average pressure is used to determine the pressure dependence of the fracture envelope. The intersect of the fracture loci with the mean stress axis denoted by p_{cutoff} in Fig. 2 indicates beyond which the material can not take any plastic deformation before fracture. The nonlinearity becomes more significant for higher compressive pressure, meanwhile, the equivalent strain at failure is difficult to measure, since the cross-sectional area becomes too small. The limiting pressure is so high that under such pressure, an existing crack can actually heal. Ideally, the strain at failure goes to infinity as the hydrostatic pressure approaches p_{lim}. A complete analysis shows that the limiting pressures for the armor steels are approximately in the range of 2–4 GPa. For soft metals, this limiting pressure can be lower. For instance, Pugh et al. (1960) showed that the limiting confining pressure is relatively low for zinc, ≈100 MPa. On the other hand, except some extreme cases, practical applications seldom reach such high compressive pressures. In the moderate hydrostatic pressure range, the obtained logarithmic relation is sufficient for practical purposes.

The first order linear approximation of Eq. (16) is

$$\varepsilon_{\text{f}} = \varepsilon_{\text{f0}} \left(1 - q\frac{p}{p_{\text{lim}}}\right). \tag{19}$$

[1] In the present paper, "log" denotes natural logarithm.

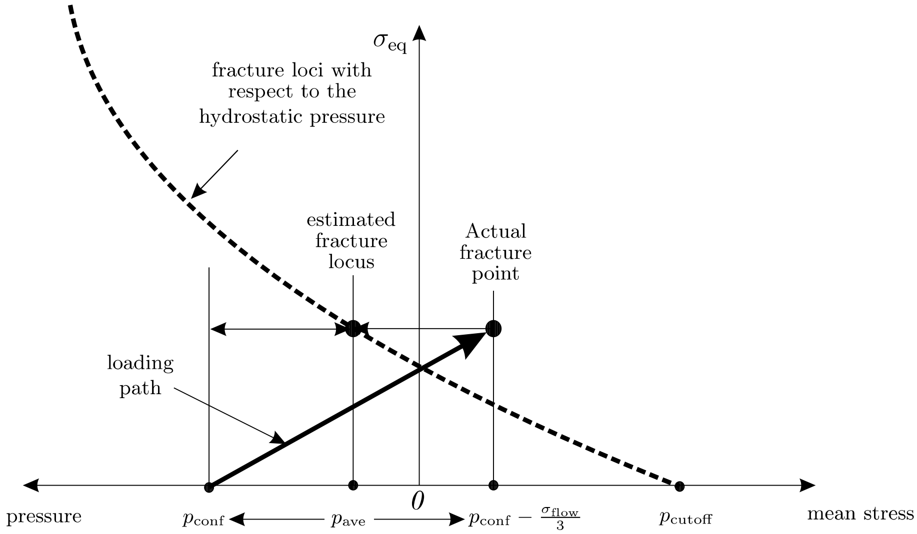

Fig. 2. An illustrative sketch of the average hydrostatic pressure experienced in the course of uniaxial pulling under a confining pressure.

Admittedly, both q and p_{lim} are sensitive to the experimental error from limited data. However, from this linearized relationship of the effective failure strain and the hydrostatic pressure, the value of $\frac{p_{lim}}{q}$ can be estimated with fairly good confidence in the pressure level of many industrial applications. A precise measurement of the fracture strain at high compressive pressure has to be assured, if nonlinearity under high pressure is of interest.

From Eq. (16), a cut-off value of tensile pressure emerges. It could be shown from Eq. (16) that the fracture strain becomes negative when the hydrostatic pressure falls below

$$p_{cutoff} = p_{lim}[1 - e^{(1/q)}]. \tag{20}$$

At this cut-off pressure, the effective failure strain ε_{f0} is zero, which means the material could not take any plastic strain.

In reality, it is difficult to design a constant pressure test for calibration purposes. For instance, the torsion tests in a pressure chamber is a constant pressure test, but there are difficulties in constructing such an apparatus (Bridgman, 1952). Using an averaging method, the loading paths with different hydrostatic pressures can be estimated from tensile tests in a pressure chamber in the negative mean stress side or from tension test of the un-notched and notched round bar in the positive mean stress side.

2.5. Lode dependence

If taking only the pressure effect into account, one might draw a conclusion that the fracture strain in simple shear is greater than that in simple tension due to the lack of hydrostatic tension. However, experiments show that sometimes the simple shear (or torsion) fracture strain can be less than the simple tension fracture strain (Bao and Wierzbicki, 2004; Halford et al., 1962; McClintock et al., 1971; Neimark, 1968; Wilkins et al., 1980). Clausing (1970) pointed out the distinct difference in the fracture strain between the round bar (axial symmetry) and the flat grooved plates (plane strain) from tests of seven ductile metals. Stress triaxiality plays a role in the transverse plane strain and the axisymmetric tension. Equal importantly is the Lode angle dependence in the distinct difference observed by Clausing. Therefore, we include a Lode angle dependence function to describe this difference.

For isotropic materials, the principal stresses are interchangeable to reflect the independence of damage to the observation frame. The Lode angle dependence function for damage evolution should have symmetry in all three principal planes. On an octahedral plane, the azimuth angle can be divided into six parts that have the same Lode angle dependence function. Each part covers the complete range of the χ from 0 to 1. Following the assumption that forward motion and backward motion induces the same amount of damage, an additional

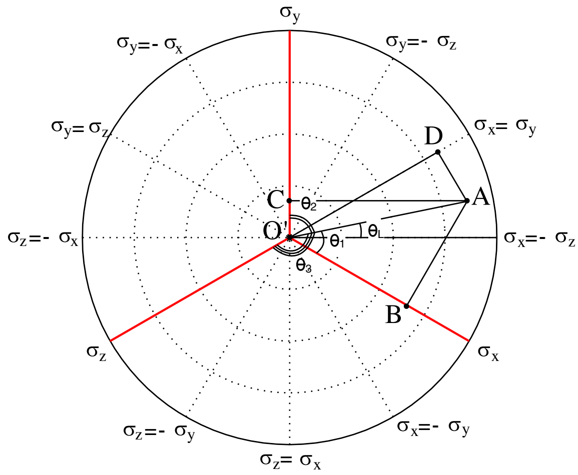

Fig. 3. The deviatoric stress state on an octahedral plane.

symmetry is introduced to the octahedral plane. In other words, the shape of the twelve segments is the same (apart from the reflections).

Based on the assumption that the effect of the hydrostatic pressure and the deviatoric state on the failure strain can be uncoupled and determined from separate series of tests, it is ideal to conduct a series of experiments that covers one sixth of the octahedral plane.

The azimuth angle can be characterized by the Lode angle θ_L (von Lode, 1925), which is defined as

$$\theta_L = \tan^{-1}\left\{\frac{1}{\sqrt{3}}\left[2\left(\frac{s_2 - s_3}{s_1 - s_3}\right) - 1\right]\right\}, \tag{21}$$

where s_1, s_2 and s_3 are the maximum, intermediate and minimum principal deviatoric stresses, respectively.

The Lode angle is also shown in Fig. 3. It is widely used in the granular material community and the influence of the Lode angle is often referred as "Lode dependence." The relative ratio of the principal stresses is used here to represent the azimuth angle θ, which is defined as the angle to the positive direction of the s_1 axis, i.e. θ_1 in Fig. 3.

The relative ratio[2] of the principal deviatoric stresses, χ, is defined as

$$\chi = \frac{s_2 - s_3}{s_1 - s_3}. \tag{22}$$

To recognize the difference between $\chi = 0.5$ and $\chi = 0$, we define a new parameter γ, which is the ratio of the fracture strain at $\chi = 0.5$ to that at $\chi = 0$ at the same constant hydrostatic pressure, i.e.

$$\gamma = \frac{\varepsilon_f(\chi = 0.5)}{\varepsilon_f(\chi = 0)}. \tag{23}$$

Due to the lack of experimental data on constant pressure paths, the Lode angle dependence function has to be constructed in a heuristic way. Here, we present two kinds of the Lode dependence functions. The first kind is a first order linear relationship in the plane of strain components, as shown in Fig. 4. The fracture point representing the fracture strain at the generalized tension or compression is connected to that of the plane strain condition by a straight line and, thus, forms a polygon on the strain plane as shown in Fig. 4 as a solid line. The "*six point star*" in Fig. 4 can be represented by the function

[2] The term "*relative ratio*" is used to describe quantities of the form $(b - c)/(a - c)$, which falls between 0 and 1 when $a \geqslant b \geqslant c$. It is adopted here to distinguish with quantity of b/a, which is the "*ratio*" of b and a.

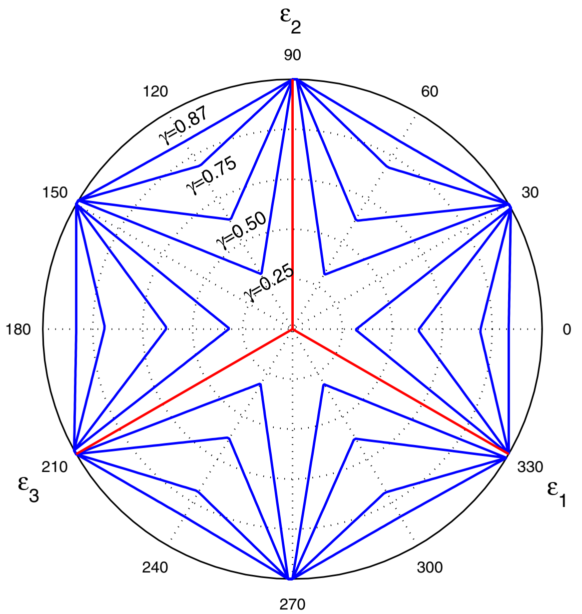

Fig. 4. The first kind of Lode dependence function of the equivalent fracture strain.

$$\mu_\theta = \begin{cases} \frac{\sqrt{\chi^2-\chi+1}}{1+\left(\frac{\sqrt{3}}{\gamma}-2\right)\chi}, & 0 \leqslant \chi \leqslant 0.5; \\ \frac{\sqrt{\chi^2-\chi+1}}{1+\left(\frac{\sqrt{3}}{\gamma}-2\right)(1-\chi)}, & 0.5 < \chi \leqslant 1, \end{cases} \tag{24}$$

which is symmetric with respect to $\chi = 0.5$. Therefore, the fracture envelope is constructed for each of the twelve pie slices on the octahedral plane, which are identified by either $0 \leqslant \chi \leqslant 0.5$ or $0.5 < \chi \leqslant 1$. As a special case, the first kind of the Lode dependence function reduces to a right hexagon when $\gamma = \frac{\sqrt{3}}{2}$.

The second kind of Lode dependence function is defined by

$$\mu_\theta = \gamma + (1-\gamma)\left(\frac{6|\theta_L|}{\pi}\right)^k, \tag{25}$$

where k is a shape parameter. The second kind of the Lode dependence function degenerates to a prefect circle when $\gamma = 1$. It should be emphasized that Figs. 4 and 5 are on the plane of the principal plastic strain components and should be distinguished from the yield surface.

Combining Eqs. (17) and (24), the fracture envelope can be expressed in the fracture strain function, i.e.

$$\varepsilon_f = \begin{cases} \varepsilon_{f0}\left[1 - q\log\left(1-\frac{p}{p_{\lim}}\right)\right]\frac{\sqrt{\chi^2-\chi+1}}{1+\left(\frac{\sqrt{3}}{\gamma}-2\right)\chi}, & 0 \leqslant \chi \leqslant 0.5; \\ \varepsilon_{f0}\left[1 - q\log\left(1-\frac{p}{p_{\lim}}\right)\right]\frac{\sqrt{\chi^2-\chi+1}}{1+\left(\frac{\sqrt{3}}{\gamma}-2\right)(1-\chi)}, & 0.5 < \chi \leqslant 1, \end{cases} \tag{26}$$

in which the fracture envelope is characterized by four material constants ε_{f0}, γ, q and $p_{\lim}$ and two stress state parameters p and χ.

Wilkins et al. (1980) suggested the Lode dependence is governed by

$$\mu_\theta = (2-A)^\beta, \tag{27}$$

where β is a material constant and A is the stress asymmetry

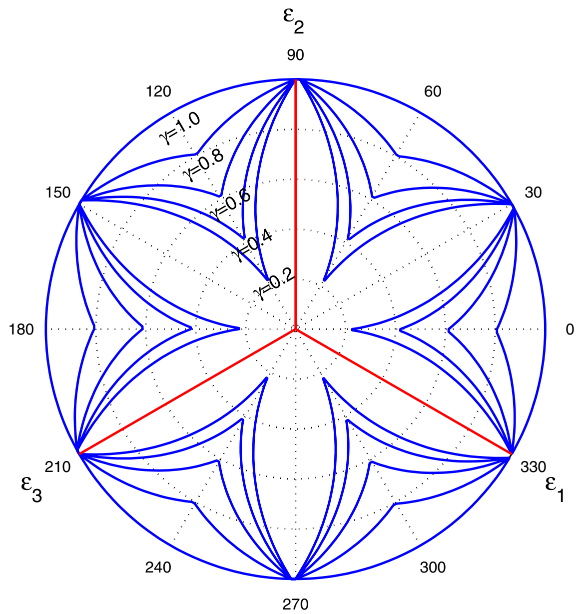

Fig. 5. The second kind of Lode dependence function of the equivalent fracture strain. Plotted here is for $k = 1$.

$$A = \max\left\{\frac{s_2}{s_1}, \frac{s_2}{s_3}\right\}. \tag{28}$$

It can be shown that the stress asymmetry and the relative ratio of the principal stresses are related by

$$\chi = \begin{cases} 2 - \frac{3(A+1)}{A+2}, & s_2 \leqslant 0; \\ 2 - \frac{3}{2+A}, & s_2 > 0. \end{cases} \quad \text{or } A = \begin{cases} \frac{1-2\chi}{1+\chi}, & 0 \leqslant \chi \leqslant \frac{1}{2}; \\ \frac{2\chi-1}{2-\chi}, & \frac{1}{2} \leqslant \chi \leqslant 1. \end{cases} \tag{29}$$

The material parameters γ and β can be related by

$$\gamma = 2^{-\beta}. \tag{30}$$

A comparison of the Lode angle dependence functions is shown in Fig. 6.

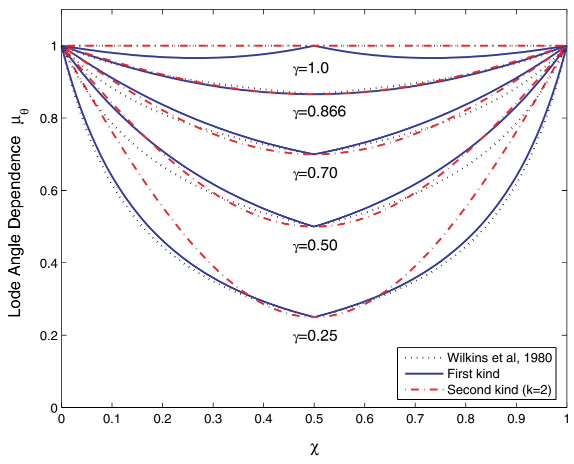

Fig. 6. A comparison of the Lode angle dependence functions.

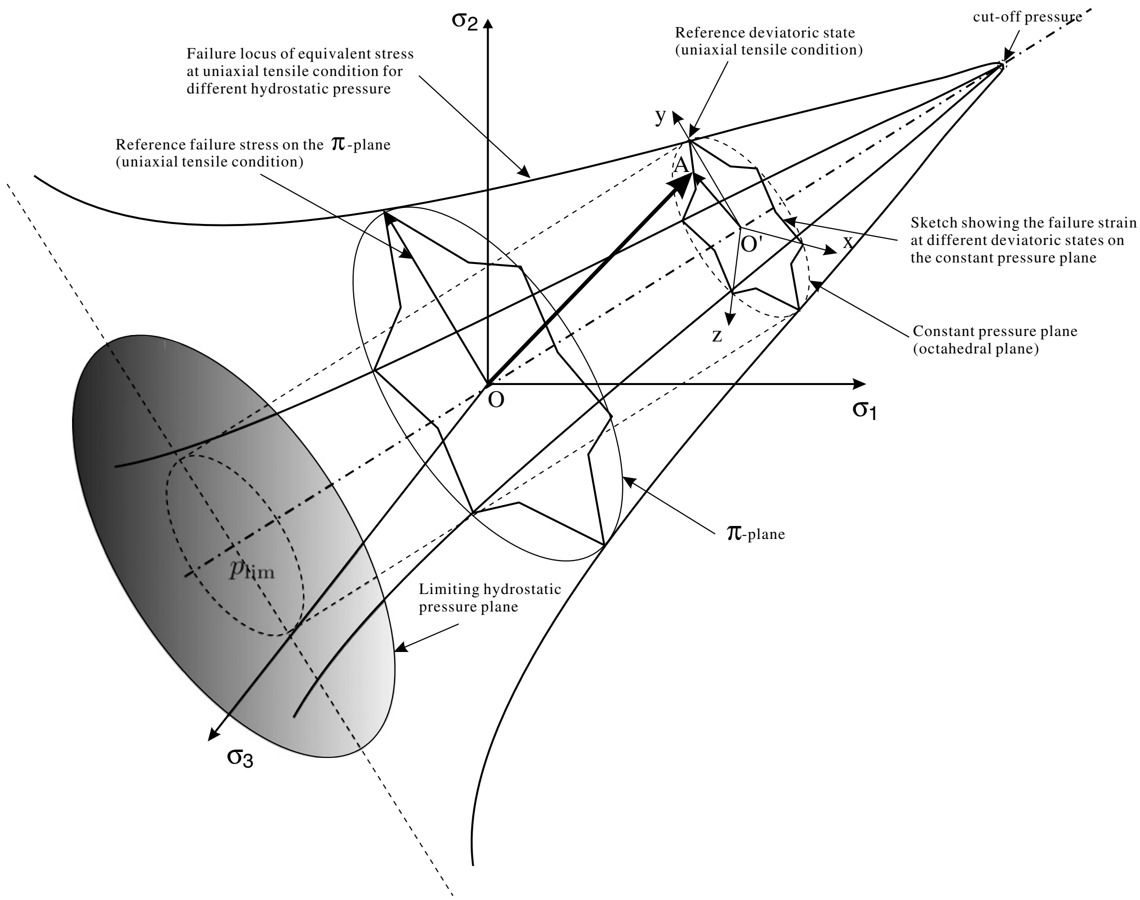

Fig. 7. A three-dimensional sketch of the fracture envelope in the space of the principal stresses.

Zhang et al. used a void containing cubic cell under prescribed loadings at different Lode parameters (Zhang et al., 2001). The applied boundary condition requires the cell remain rectangular and thus they obtained an upper bound of the response. Similar results was obtained by Kim et al. (2004).

Expressing the fracture envelope in the principal stress space, the combined effects of the hydrostatic pressure and the deviatoric state are shown in Fig. 7, which appear to be a "*blossom*." For each sextant of the fracture envelope, Wierzbicki and Xue (submitted) also provided a non-dimensional form of the fracture locus in the space of the stress invariants for proportional loadings.

2.6. Comparison with several existing models

In summary, a damage plasticity model is developed to incorporate the pressure sensitivity and the Lode angle dependence through the so-called "*cylindrical decomposition*." A nonlinear damage evolution law and the damage associated material weakening are also taken into account. Individual effects are considered in existing fracture prediction models. It is thus desired to compare the present model with existing ones. A comparison of several representative models is shown in Table 1. The considered effects in the individual models are marked.

3. A special case of the plane stress condition

The plane stress condition offers a special set of problems that has been extensively studied experimentally, analytically and numerically. Due to the absence of the normal stress, the relative ratio of the principal stresses χ is related to the ratio of the two nonzero in-plane principal stresses α, i.e.

Table 1
Comparison of the present model with several existing models for fracture prediction

	Pressure*	Lode angle	Damage rule	Weakening
Johnson and Cook (1985)	●		◑	
Wilkins et al. (1980)	●	●	◑	
Lemaître (1985)	●		●	●
Gurson–Tvergaard–Needleman	●		●	●
present model	●	●	●	●

* A filled circle "●" indicates a dependence. A half filled circle "◑" indicates a proportional linear damage rule. For Johnson-Cook model, the damage is assumed to be linearly related to the plastic strain on a proportional loading path. For Wilkins model, the damage is assumed to be linearly related to the proportional deviatoric loading path.

$$\alpha = \begin{cases} 1-\chi & \sigma_1, \leqslant \sigma_2 \leqslant 0 \\ \frac{\chi-1}{\chi}, & \sigma_1 \leqslant 0 \leqslant \sigma_2 \\ \chi, & 0 \leqslant \sigma_1 \leqslant \sigma_2. \end{cases} \tag{31}$$

The range of the stress ratio, the relative ratio of the principal stresses and the stress triaxiality are illustrated in the top-left half plane. The bottom-right half plane is symmetric with respect to the line identified by $\sigma_x = \sigma_y$.

For fracture under plane stress proportional loadings, the effective failure strain can be equally expressed in one of the three parameters. From Fig. 8, the σ_x–σ_y plane is divided into six sections of full coverage of χ from 0 to 1. These six sections are each of the halves of the first and third quadrants and the second and the fourth quadrant. Meanwhile, the same plane is divided into equal halves by line $\sigma_x = \sigma_y$, each covering stress triaxiality η from $-\frac{2}{3}$ to $\frac{2}{3}$. Therefore, the joint effects of the Lode angle and the stress triaxiality on the fracture strain can be determined on any proportional loading paths in each of these six sections. This results in a garland curve on the plane of the fracture strain versus the stress triaxiality. For example, the equivalent fracture strain is plotted versus the stress triaxiality in Fig. 9 for 2024-T351 aluminum alloy.

The solid line in Fig. 9 denotes the plane stress fracture locus. In Fig. 9, the upper dash-dot line represents the fracture locus of axisymmetric loading conditions ($\chi = 0$) and the low dash-dot line represents that of plane strain conditions ($\chi = 0.5$). For proportional loading conditions other than these two extreme conditions, the fracture locus falls in-between these two bounds.

Experimental data are also plotted in Fig. 9 for aluminum alloy 2024-T351. The right three points (denoted by triangles) of experimental data in Fig. 9 are from un-notched and notched round bars and the rests

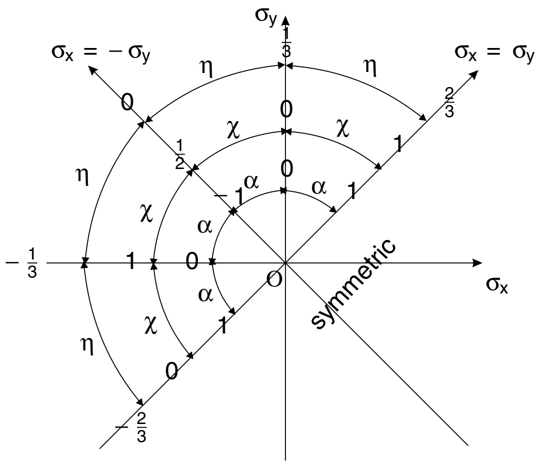

Fig. 8. The in-plane stress ratio, the relative ratio of the principal stresses and the stress triaxiality in the plane stress condition.

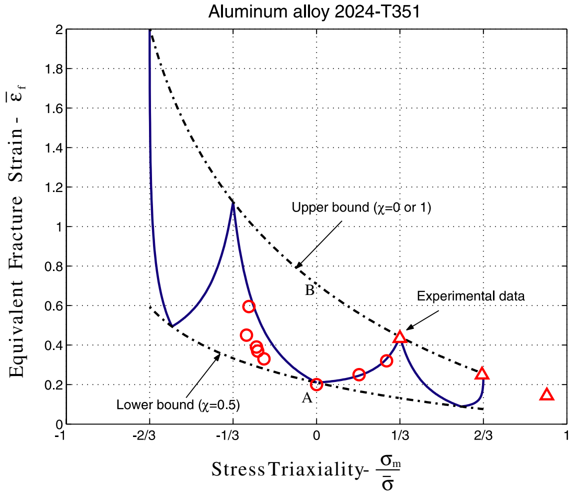

Fig. 9. The equivalent fracture strain versus the stress triaxiality for the plane stress condition. Experimental data from Bao and Wierzbicki (2004).

Table 2
Material constants for fracture characterization of 2024-T351 aluminum alloy

ε_{f0}	$p_{\lim}$	q	γ	m
0.70	925.7 MPa	1.75	0.4	1.73

(denoted by circles) are close to plane stress condition. Bao and Wierzbicki's tests locate at the middle portion of the three branches. The positive side of stress triaxiality are from tension tests of different shapes and the negative side of stress triaxiality are from upsetting tests. The upper bound shown in Fig. 9 is fitted from the axisymmetric tests.

The material parameter γ, which is the ratio of the fracture strain at $\chi = 0.5$ and $\chi = 0$ at same constant pressure, can be determined from Fig. 9. The point of intersection of this upper bound and the vertical axis $\frac{\sigma_m}{\sigma_{eq}} = 0$ (denoted by point "B") corresponds to the reference generalized tension condition, where the pressure is constant zero along the loading path. Point "B" defines the value of the reference fracture strain ε_{f0}. The nonlinear parameters $p_{\lim}$ and q are also obtained from the fitting of the upper bound. The ratio of the simple shear fracture strain (denoted by point "A") and ε_{f0} defines the fracture strain ratio at plane strain condition to generalized tension condition, i.e. the material constant γ. For aluminum alloy 2024-T351, it appears that the material is Lode angle sensitive. For simple shear case, the fracture strain is only 0.2. From the extrapolation of the fracture loci from round bar specimens, the intersection (point B) indicates $\varepsilon_{f0} = 0.7$. Therefore, $\gamma = 0.29$. Batra et al. (1995) showed the fracture strain of AA 2024-T351 in torsion is about 0.4, which indicates a larger $\gamma = 0.57$. In the present study, we choose an intermediate value of $\gamma = 0.4$. The complete set of five parameters for the fracture envelope is listed in Table 2.

4. Numerical validation

The proposed model is implemented into a commercial code LS-DYNA as a user defined material model. Backward Euler method is used in the numerical integration scheme (Xue, 2007). Several numerical calculations for representative load conditions have been performed. These calculations include (a) an un-notched round bar in axial tension; (b) a doubly grooved flat plate (transverse plane strain); (c) a dog-bone plane stress coupon in tensile test and (d) a compact tension test. In all these cases, the specimens are pulled at both ends in the vertical direction. Some other simulation results are reported in Xue (2007); Xue et al. (2006). The stress–strain curve for the matrix material is shown in Fig. 10.

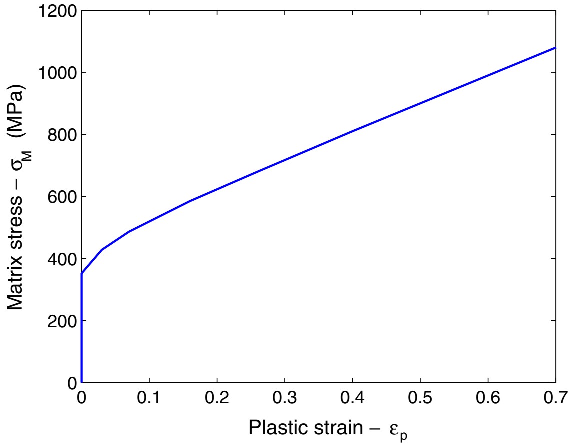

Fig. 10. The approximate stress–strain curve for the matrix material of aluminum alloy 2024-T351.

4.1. Un-notched axisymmetric round bar

The uniaxial tension of an un-notched round bar is often used as a standard test to determine the material strength. For ductile metals, the specimen usually forms a localized neck before final fracture occurs. Careful examination of the microstructure at the neck reveals that the fracture starts at the center of the neck and propagates towards the free outer surface. The initial crack is in tensile mode and is perpendicular to the loading direction. The crack propagates until a large shear lip occurs (Puttick, 1959; Rogers, 1960). A ‘‘cup-cone’’ shaped fracture surface is thus formed.

The numerical calculation shows a realistic ‘‘cup-cone’’ fracture mode as shown in Fig. 11. Similar results were obtained by Tvergaard and Needleman (1984), Besson et al. (2001) using Gurson-like model (Gurson, 1977) and more recently by Scheider and Brocks (2003) using cohesive model. In the present study, the proposed damage plasticity model is applied. The simulation is performed using axisymmetric brick elements. The un-notched round bar has a diameter of 9 mm and is discretized using 0.1 mm by 0.1 mm elements at the middle section. The crack propagation is shown in Fig. 11.

As the crack propagates toward to free outer surface, the plastic deformation localizes in two shear bands, which forms shear lips. The simulation results show that the inclination angle of the deviatoric state, strain rate and the damage rate in the shear bands are different. The differences in the inclination angles are shown in Fig. 12. The contour lines of the deviatoric state χ shows the values of χ in these bands are between 0.4 and 0.5 and these bands are inclined towards the cross-sectional plane about 57°, as shown in Fig. 12(a). The inclination angle of the localized bands of the plastic strain rate is about 46°, as shown in Fig. 12(b). The joint

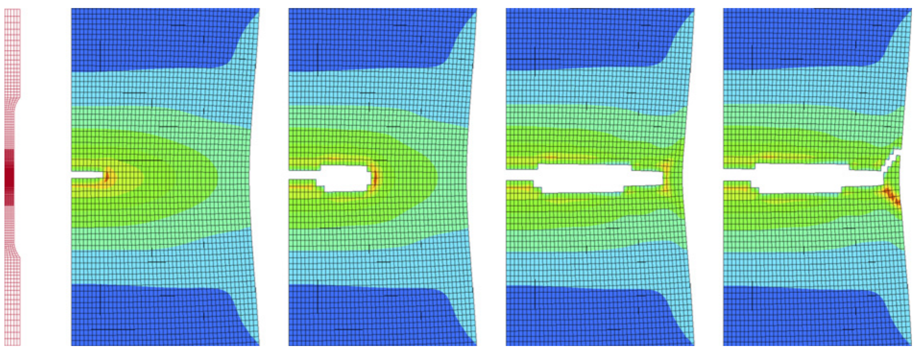

Fig. 11. A cup-cone fracture mode is observed in the un-notched round bar (left, finite element mesh; right, propagation of the crack. Plotted are the contours of damage).

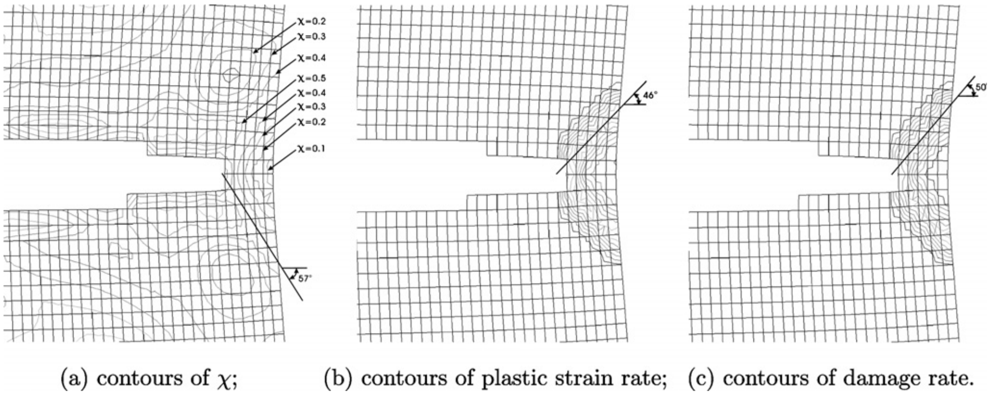

Fig. 12. The formation of shear lips. The differences in the inclination angles of χ, the plastic strain rate and the damage rate are shown. (a) Contours of χ; (b) contours of plastic strain rate; (c) contours of damage rate.

effects of χ and the plastic strain rate results in an inclination angle of 50° of the damage rate bands, as shown in Fig. 12(c).

4.2. Doubly grooved flat plate (transverse plane strain)

The stress condition in transverse plane strain loading is a shear loading superimposed by a hydrostatic tension. Experiments show the crack usually propagates in the direction of the maximum shear in this case. The doubly grooved flat plate is often used to study the plane strain in tension, e.g. Clausing (1970). The grooves are perpendicular to the loading direction. At large deflection, two distinct shear bands at an angle of ≈45° to the loading direction appeared at the grooved section of the plate. The fracture mode of the doubly grooved flat plate is dominated by a slant fracture (or sometimes a symmetric chevron-type of crack (Besson et al., 2003). This slant fracture is shown in Fig. 13. In this calculation, the grooved section is 3 mm wide and 6 mm tall and is descritized by plane strain brick elements of size 0.1 mm by 0.1 mm.

4.3. Tensile flat specimen

The third example is a tensile flat coupon test. The width of the center section is 20 mm and is discretized using 0.33 mm by 0.33 mm shell elements. The localized necking follows the diffused necking and then fracture initiates at the center of the neck. The contour lines of damage at the neck are plotted on the right side of Fig. 14 at the onset of fracture. It is found that the damage accumulated faster at the two preferred directions, which are inclined to the loading direction at an angle of 55°. This inclination angle agrees with theoretical analysis (Hill, 1952; McClintock and Zheng, 1993). The final crack forms in one of the two damage bands, as shown on the right side of Fig. 14.

4.4. Compact tension specimen

A slant fracture surface is often found in the compact tension specimen in certain range of thickness (Anderson, 1995; James and Newman, 2003; Mahmoud and Lease, 2003; Rivalin et al., 2001). Three-dimensional calculations have been performed to simulate the crack propagation of a compact tension test (Dawicke et al., 1995; Mahmoud and Lease, 2004; Mathur et al., 1996). Because of the constraint of normal stress at the symmetric plane, the center of the crack tip is close to plane strain condition. However, the normal stress reduces to zero at the surface. The plastic fracture process zone is in a triaxial stress zone ahead of the creak tip. Therefore, a full three dimensional simulation is necessary to simulate the crack tip behavior in a compact tension specimen (Xue et al., 2006). The finite element model of the compact tension specimen with $a/W = 0.5$ and width $W = 50.8$ mm is shown Fig. 15. A realistic slant fracture model is predicted, as shown in Fig. 16.

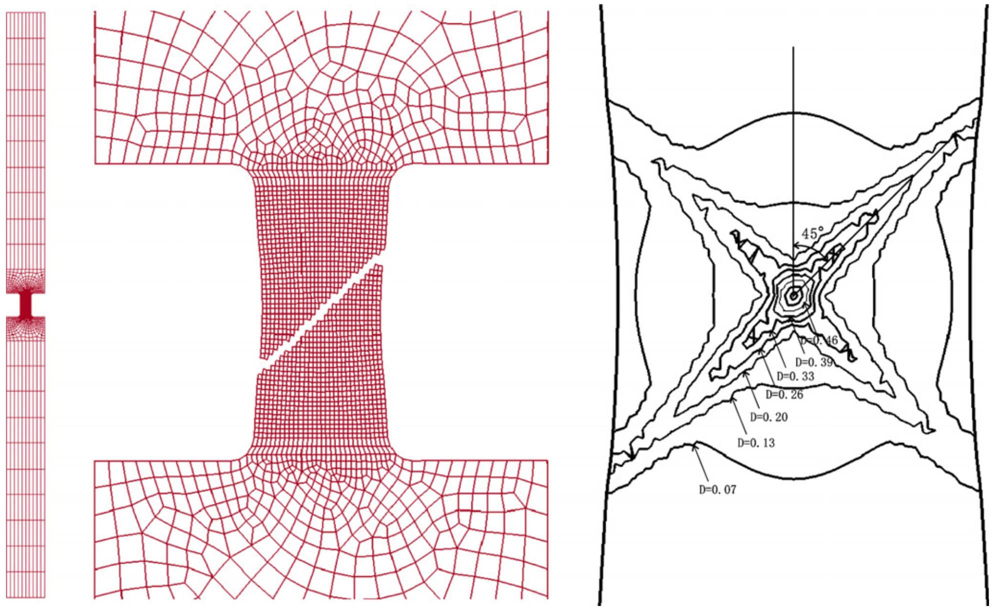

Fig. 13. A 45° slant crack is observed in the flat grooved plate (left, overall cross-section; middle, slant crack at the grooved section; right, contour lines of damage just before fracture occurs).

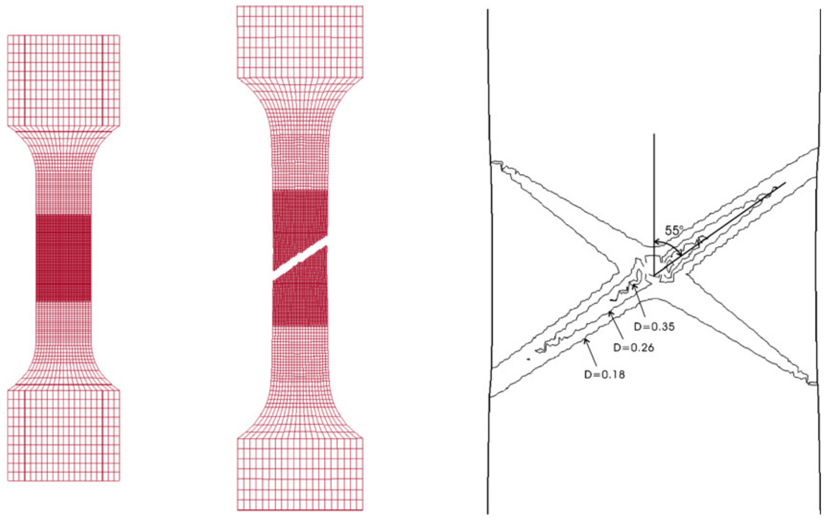

Fig. 14. A slant crack is observed for thin-walled flat dog-bone tensile specimen (left, before test; middle, after test; right, contour lines of damage at the neck).

Xue et al. (2006) also showed that the synegistic effects of the combination of the Lode angle dependence and the material weakening favor a slant fracture mode.

5. Conclusions

A damage plasticity model is proposed in the present paper. The ductile damage is induced by the plastic deformation and leads to ultimate fracture. The material properties are characterized by a set of constitutive equations describing damage evolution and material deterioration. In the present paper, damage is defined as the relative loss of the deformability. The damage evolution is given in the rate form through a "*cylindrical*

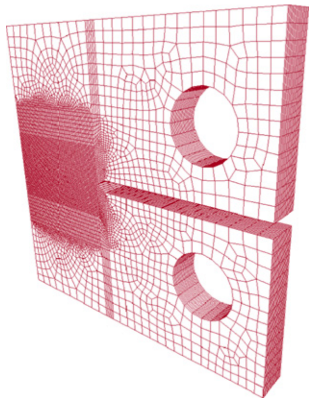

Fig. 15. The finite element mesh of a compact tension specimen.

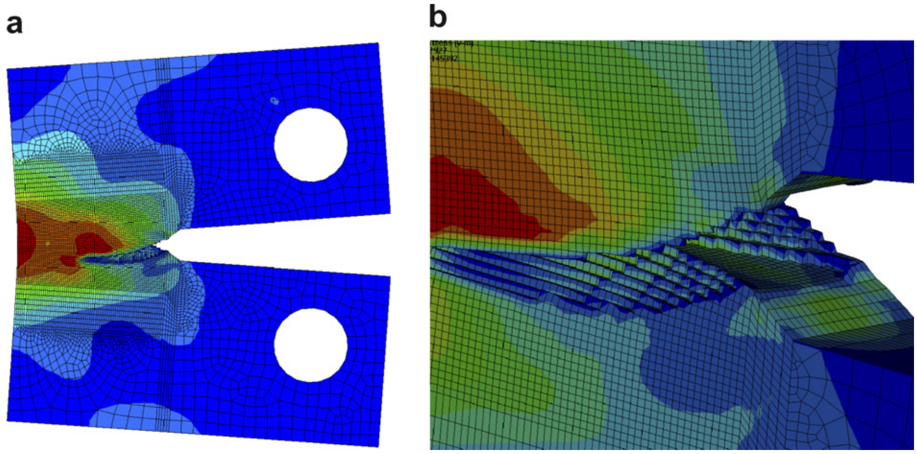

Fig. 16. The predicted slant fracture mode of a compact tension specimen (After Xue et al. (2006)). The von Miese equivalent stress contours are plotted. (a) Fractured specimen; (b) Slant crack propagation.

decomposition'' of damage by incorporating the pressure dependence, the Lode angle effect and a power law damage rule. The material fracture occurs when the accumulated damage reaches unity.

While the hydrostatic pressure and the Lode angle may have joint effects, it is assumed in the present model that these two effects are independent and can be calibrated separately. The Lode angle dependence is simplified as a ''*six point star*'' on the plastic strain plane. The combined pressure and Lode angle effects result in a ''*blossom*'' shaped fracture envelope in the principle stress space. The fracture envelope can be described by a set of four parameters, viz. ε_{f0}, $p_{\lim}$, q and γ, which can be calibrated through laboratory experiments. Furthermore, a damage exponent m is adopted to describe the nonlinear damage accumulation effect. Four numerical calculations are given to illustrate the capability of the proposed model in predicting crack paths.

It is recognized that the relationships in describing the pressure sensitivity, the Lode angle dependence and the damage accumulation are phenomenological in nature. More data are in need to better define these relationships. A deliberate experimental program is being conducted. The test results and the numerical comparison will be used to further justify the present method.

Acknowledgement

The author is grateful to Professor T. Wierzbicki and Dr. X. Teng for their valuable comments. The author is also grateful to the Referees for their detailed reviewing and constructive suggestions. Support of this work came in part from the ONR/MURI award to MIT and the NNR initiative through the Office of Naval Research.

References

Anderson, T.L., 1995. Fracture Mechanics: Fundamentals and Applications. CRC Press, Boca Raton.
Bao, Y., Wierzbicki, T., 2004. On fracture locus in the equivalent strain and stress triaxiality space. International Journal of Mechanical Sciences 46, 81–98.
Batra, R.C., Zhang, X., Wright, T.W., 1995. Critical strain ranking of 12 materials in deformations involving adiabatic shear bands. Journal of Applied Mechanics – Transactions of ASME 62, 252–255.
Besson, J., Steglich, D., Brocks, W., 2001. Modeling of crack growth in round bars and plane strain specimens. International Journal of Solids and Structures 38 (46-47), 8259–8284.
Besson, J., Steglich, D., Brocks, W., 2003. Modeling of plane strain ductile rupture. International Journal of Plasticity 19, 1517–1541.
Bonora, N., Newaz, G.M., 1998. Low cycle fatigue life estimation for ductile metals using a nonlinear continuum damage mechanics model. International Journal of Solids and Structures 35 (16), 1881–1894.
Børvik, T., Hopperstad, O.S., Berstad, T., Langseth, M., 2001. A computational model of viscoplasticity and ductile damage for impact and penetration. European journal of mechanics. A, Solids 20, 685–712.
Bridgman, P.W., 1952. Studies in large plastic flow and fracture. McGraw-Hill.
Clausing, D.P., 1970. Effect of plastic strain state on ductility and toughness. International Journal of Fracture Mechanics 6 (1), 71–85.
Cockcroft, M.G., Latham, D.J., 1968. Ductility and the workability of metals. Journal of the Institute of Metals 96, 33–39.
Coffin Jr., L.F., 1954. A study of the effects of cyclic thermal stresses on a ductile metal. Transactions of American Society of Mechanical Engineers 76, 931–950.
Coffin Jr., L.F., 1958. Cyclic straining and fatigue. In: Proceedings of the symposium on internal stresses and fatigue in metals. Detroit and Warren, MI, pp. 363–381.
Coffin Jr., L.F., Tavernelli, J.F., 1959. The cyclic straining and fatigue of metals. Transactions of the Metallurgical Society of AIME 215, 794–807.
Coffin, L.F. Jr.. An investigation of the cyclic strain and fatigue behaviour of a low-carbon manganese steel at elevated temperature. In Thermal and High-Strain Fatigue, Proceedings of an International Conference organized by the Institute of Metals in association with the Iron and Steel Institute, pp. 171–197, Church House, London, 6–7 June 1967.
Dawicke, D.S., Newman Jr., J.C., Bigelow, C.A., 1995. Three-dimensional CTOA and constraint effects during stable tearing in a thin-steel material. Fracture Mechanics: ASTM STP 1256 26, 223–242.
Gurson, A.L., 1977. Continuum theory of ductile rupture by void nucleation and growth: Part I. Yield critetria and flow rules for porous ductile media. Journal of Engineering Materials and Technology 99, 2–15.
Halford, G.R., Morrow, J. On low-cycle fatigue in torsion, volume 62 of American Society for Testing and Materials proceedings, pp. 695–707. American Society for Testing and Materials, 1962.
Hancock, J.W., Mackenzie, A.C., 1976. On the mechanisms of ductile failure in high-strength steels subjected to multi-axial stress-states. Journal of the Mechanics and Physics of Solids 24 (2-3), 147–160.
Hill, R., 1952. On discontinuous plastic states, with special reference to localized necking in thin sheets. Journal of the Mechanics and Physics of Solids 1, 19–30.
Holland, D., Halim, A., Dahl, W., 1990. Influence of stress triaxiality upon ductile crack propagation. Steel Research 61 (10), 504–506.
James, M.A., Newman Jr., J.C., 2003. The effect of crack tunneling on crack growth: experiments and CTOA analysis. Engineering Fracture Mechanics 70, 457–468.
Johnson, G.R., Cook, W.H., 1985. Fracture characteristics of three metals subjected to various strains, strain rates, temperatures and pressures. Engineering Fracture Mechanics 21 (1), 31–48.
Kachanov, L.M., 1958. On the creep fracture time. Izv. Akad. Nauk USSR Otd. Tekh. 8, 26–31 (in Russian).
von Karman, T., 1911. Strength investigations under hydrostatic pressure. Zeitschrift des Verines Deutscher Ingenieure 55, 1749–1757.
Kim, J., Gao, X., Srivatsan, T.S., 2004. Modeling of void growth in ductile solids: effects of stress triaxiality and initial porosity. Engineering Fracture Mechanics 71, 379–400.
Lemaître, J., Chaboche, J.L., 1978. Aspect Phénomènologique de la Rupture par Endommagement. Journal de Mécanique Appliquée 2, 317–365.
Lemaître, J., 1985. A continuous damage mechanics model for ductile fracture. Journal of Engineering Materials and Technology 107, 83–89.
Lemaître, J., 1992. A Course on Damage Mechanics. Springer, Berlin, New York.
Lemaître, J., Dufailly, J., 1987. Damage measurements. Engineering Fracture Mechanics 28 (5-6), 643–661.
Lewandowski, J.J., Lowhaphandu, P., 1998. Effect of hydrostatic pressure on mechanical behavior and deformation processing of materials. International Materials Reviews 43 (4), 145–187.
Libertiny, G.Z., 1967. Effect of hydrostatic pressure on the short life fatigue property of an alloy steel. the Institution of Mechanical Engineers 182 (3C), 48–64.
von Lode, W., 1925. Versuche über den einflu*β* der mittleren hauptspannug auf die flie*β*grenze. Zeitschrift für angewandte mathematik und mechanik 5 (2), 142–144.
Mahmoud, S., Lease, S., 2003. The effect of specimen thickness on the experimental characterization of critical crack-tip-opening angle in 2024-t351 aluminum alloy. Engineering Fracture Mechanics 70, 443–456.

Mahmoud, S., Lease, K., 2004. Two-dimensional and three-dimensional finite element analysis of critical crack-tip-opening angle in 2024-T351 aluminum alloy at four thickness. Engineering Fracture Mechanics 71, 1379–1391.

Manson, S.S. Behavior of materials under conditions of thermal stress. Technical Report NACA-TR-1170, National Advisory Committee for Aeronautics, 1954.

Manson, S.S., Hirschberg, M.H. Fatigue behavior in strain cycling in the low- and intermediate-cycle range. In Fatigue – An Interdisciplinary Approach, Proceedings of the 10th Sagamore Army Research Conference, Raquette Lake, NY, 13–16 August 1963.

Mathur, K.K., Needleman, A., Tvergaard, V., 1996. Three dimensional analysis of dynamic ductile crack growth in a thin plate. Journal of the Mechanics and Physics of Solids 44 (3), 439–464.

McClintock, F.A., 1968. A criterion for ductile fracture by growth of holes. Trans. ASME. Journal of Applied Mechanics 35, 363–371.

McClintock, F.A. Plasticity aspects of fracture, volume III of Fracture An Advanced Treatise, chapter 2, pp. 47–307. Academic Press, New York and London, 1971.

McClintock, F.A., Zheng, Z.M., 1993. Ductile fracture in sheets under transverse strain gradients. International Journal of Fracture 64, 321–337.

Mogi, K., 1967. Effect of the intermediate principal stress on rock failure. Journal of Geophysical Research 72 (20), 5117–5131.

Mogi, K., 1972. Effect of the triaxial stress system on fracture and flow of rocks. Physics of the Earth and Planetary Interiors 5, 318–324.

Neimark, J.E., 1968. The fully plastic, plane-strain tension of a notched bar. Journal of Applied Mechanics, pages, 111–116.

Norris, D.M., Reaugh, J.E., Moran, B., Quinnones, D.F., 1978. A plastic-strain mean-stress criterion for ductile fracture. Journal of Engineering Materials 100, 279–286.

Osgood, C.C., 1982. Fatigue Design, 2nd ed. Pergamon Press, New York.

Pugh, H.Ll.D. Cold deformation of metals part 2 – cold extrusion. Metal Treatment and Drop Forging, pp. 231–236, June 1960.

Puttick, K.E., 1959. Ductile fracture in metals. Philosophical magazine 4, 964–969.

Rivalin, F., Pineau, A., Di Fant, M., Besson, J., 2001. Ductile tearing of pipeline-steel wide plates I: dynamic and quasi-static experiments. Engineering Fracture Mechanics 68, 329–345.

Rice, J.R., Tracey, D.M., 1969. On the ductile enlargement of voids in triaxial stress fields. Journal of the Mechanics and Physics of Solids 17, 201–217.

Rogers, H.C., 1960. Tensile fracture of ductile metals. Transactions of Metallurgical Society of AIME 218, 498–506.

Scheider, I., Brocks, W., 2003. Simulation of cup-cone fracture using the cohesive model. Engineering Fracture Mechanics 70 (14), 1943–1961.

Spitzig, W.A., 1990. Effect of hydrostatic pressure on deformation, damage evolution, and fracture of iro with various initial porosities. Acta Metallurgica et Materialia 38 (8), 1445–1453.

Suresh, S., 1998. Fatigue of Materials. Cambridge University Press.

Tvergaard, V., Needleman, A., 1984. Analysis of the cup-cone fracture in a round tensile bar. Acta Metallurgica 32 (1), 157–169.

Wierzbicki, T., Xue, L. On the effect of the third invariant of the stress deviator on ductile fracture. Submitted for publication.

Wilkins, M.L., Streit, R.D., Reaugh, J.E. Cumulative-strain-damage model of ductile fracture: Simulation and prediction of engineering fracture tests. Technical Report UCRL-53058, Lawrence Livermore National Laboratory, October 1980.

Xue, L., 2007. Ductile fracture modeling – theory, experimental investigation and numerical verification. Ph.D. dissertation, Department of Mechanical Engineering, Massachusetts Institute of Technology.

Xue, L., Wierzbicki, T. Ductile fracture initiation and propagation modeling using a new fracture criterion. In Besson, J., Moinereau, D., Steglich, D. (Eds.), Local Approach to Fracture, Proceedings of the 9th European Mechanics and Materials Conference, Moret-sur-Loing, France, May 9–12, 2006.

Zhang, K.S., Bai, J.B., François, D., 2001. Numerical analysis of the influence of the Lode parameter on void growth. International Journal of Solids and Structures 38, 5847–5856.